Bandgap analysis of periodic composite microplates using curvature-based flexoelectricity: a finite element approach

P Y Lai, Z Z He, Y. Cong, S.T. Gu, G. Y. Zhang

Bandgap analysis of periodic composite microplates using curvature-based flexoelectricity: a finite element approach

P. Y. Lai,[1] Z. Z. He,[2] Y. Cong,[3,*] S. T. Gu,[1,] G. Y. Zhang[2]**

[1] *School of Civil Engineering, Chongqing University, Chongqing 400044, China.*

[2] *Jiangsu Key Laboratory of Engineering Mechanics, School of Civil Engineering, Southeast University, Nanjing, Jiangsu 210096, China.*

[3] *University Paris-Saclay, Univ Evry, LMEE, 91020, Evry, France.*

ABSTRACT

A finite element model is proposed permitting prediction of elastic wave bandgaps of periodic composite microplates incorporating flexoelectric effect. In this model, we applied curvature-based flexoelectricity and Mindlin plate theories and derived a finite element formulation that has been implemented for bandgap analysis. The finite element model utilizes a three-node triangle element with 30 degrees of freedom satisfying Mindlin kinematics assumptions. It is based on a non-conforming interpolation scheme which provides nodal C^1 continuity and ensures compatibility with curvature-based flexoelectricity. The approach accounts for microstructure effects and, owing to the triangular element topology, can be used to assist the design of microplates with complex microstructures. Validation of the approach is performed through comparison with both analytical and numerical models, in which the effect of flexoelectricity on the bandgap is studied based on cases demonstrating size dependence. In the end, an application of the proposed model is provided where bandgap properties of an anti-tetrachiral metastructure are investigated.

Keywords: Bandgap; Curvature-based flexoelectricity; Mindlin plate; Wave propagation; Metamaterial design; Finite element

1. Introduction

Bandgap materials [1] refer to a class of natural or artificially designed materials that present unusual characteristics in attenuating wave propagation as function of frequency. Among such materials, an important number is composed of composite microplates with periodic

* Corresponding author. E-mail: yu.cong@univ-evry.fr (Y. Cong)

** Corresponding author. E-mail: gust@cqu.edu.cn (S. T. Gu)

microstructures [2-3] and has been increasingly investigated for advanced applications such as vibration controllers, energy harvesters, micro scale waveguides etc. [4-6].

On small scales, the design of composite microstructures increasingly involves integration of functional materials with electromechanical coupling, for which flexoelectricity, a two-way coupling [7-9] between polarization and strain gradient [10], represents a general phenomenon in all dielectrics. Despite its weak influence on behaviors of bulk materials, flexoelectricity may significantly impact the behaviors of micro- to nano-scale structures for which the size-dependent effect of strain gradient becomes non negligible. In the area of finite element modelling, integration of flexoelectricity usually requires implementation of higher-order theories of elasticity since second-order derivatives of displacement is involved. Successful implementations using this strategy include the application of strain gradient theories (e.g., [12-16]) and couple stress theories (e.g., [17-18]). In this regard, Yvonnet *et al.* [12] investigated a 2-D numerical framework for characterizing the flexoelectric effect in soft dielectrics with finite strains by using Argyris triangular element [19] that provides C^1 element continuity. Deng *et al.* developed 2-D [13] and 3-D [14] mixed finite elements that offer an alternative solution to satisfy the continuity requirement. In the area of layered structures, modelling of flexoelectric effect has been investigated based on strain gradient elasticity [15,16]. However, difficulties subsist in determining strain gradient-based flexoelectric constants. To remedy this issue and provide a flexoelectric model with minimal additional parameters, many efforts have been made recently to elaborate couple stress based flexoelectric models. These efforts have led to the theory of curvature-based flexoelectricity [17,18], yet only analytical models have been proposed with limited applications involving simple problem geometries. Therefore, a finite element implementation of the curvature-based flexoelectricity theory would be of particular interest, permitting simulations of microstructures with complex geometries on the small scale.

In this paper, we base our work on a three-node triangle Mindlin plate finite element with 27 DOFs. Recently investigated by Xia *et al.* [20], this element utilizes non-conforming interpolation and provides nodal C^1 continuity that ensures compatibility with curvature-based flexoelectricity. An additional set of three DOFs for the discretization of electric potential field requires to be implemented to meet the requirements of flexoelectric constitutive relations. Upon implementation of the finite element model, we will explore the influence of flexoelectric effects on bandgap properties of composite microplates, which has not been investigated in the literature.

Contents of this paper is organized as follows: we briefly review in Section 2, the curvature-based flexoelectricity theory and describe the basic equations in terms of Mindlin kinematics assumptions and electric potential relations. Based on these relations, weak form of the equilibrium permitting calculation of eigenfrequencies will be given. In Section 3, we describe finite element discretization and introduce the relations regarding the transfer matrix method.

Bloch boundary conditions allowing for unit cell bandgap calculations will be given. In Section 4, we present four numerical examples to validate the proposed model: first, we validate the model by comparing with analytical calculations and confirm the presence of flexoelectric effects on composite microplates. We then study its dependence on the microstructure and upon validation of the model, an application is provided where bandgap properties of an anti-tetrachiral metastructure are investigated. Finally, the work presented in the paper will be summarized in Section 5.

2. Theoretical framework

2.1 Curvature-based flexoelectricity theory

Let us consider an electro-elastic centrosymmetric cubic material continuum that occupying a volume Ω and exhibiting microstructure and flexoelectric effects. The relative Gibbs free energy G based on the curvature-based flexoelectricity theory ([17], Qu et al. 2021) reads

$$G=\frac{1}{2}\int_{\Omega}(\boldsymbol{\sigma}:\boldsymbol{\varepsilon}+\ \mathbf{m}:\boldsymbol{\chi}-\ \mathbf{D}\cdot\ \mathbf{E})\mathrm{d}V\,, \tag{1}$$

where $\boldsymbol{\sigma}$ and $\mathbf{m}$ are the Cauchy stress and couple stress tensors, respectively. $\mathbf{D}$ refers to the electric displacement vector, and $\mathrm{d}V$ the elementary volume. Then, the strain tensor $\boldsymbol{\varepsilon}$, curvature tensor $\boldsymbol{\chi}$, and electric field intensity vector $\mathbf{E}$ are, respectively, expressed as follows:

$$\begin{aligned}&\boldsymbol{\varepsilon}=\frac{1}{2}\left[(\nabla\mathbf{u})+(\nabla\mathbf{u})^{\mathrm{T}}\right],\\&\boldsymbol{\chi}=\nabla\boldsymbol{\theta},\\&\mathbf{E}=-\nabla\varphi,\end{aligned} \tag{2}$$

where $\mathbf{u}$ is the displacement vector, $\boldsymbol{\varphi}$ is the electric potential, and $\boldsymbol{\vartheta}$ is the rotation vector defined by

$$\boldsymbol{\theta}=\frac{1}{2}\nabla\times\mathbf{u}\,. \tag{3}$$

The corresponding constitutive equations with small deformation for centrosymmetric cubic materials can be written as

$$\begin{aligned}&\boldsymbol{\sigma}=\mathbf{C}^{\mathbf{e}}:\boldsymbol{\varepsilon},\\&\mathbf{m}=-\mathbf{E}\cdot\mathbf{f},\\&\mathbf{D}=\mathbf{e}\cdot\mathbf{E}+\mathbf{f}:\boldsymbol{\chi},\end{aligned} \tag{4}$$

where $\mathbf{C}^{\mathbf{e}}$ are the fourth-order elastic stiffness tensors, $\mathbf{f}$ is the third-order flexoelectric coefficient tensor, and $\mathbf{e}$ is the second-order dielectric tensor. The matrices $\mathbf{C}^{\mathbf{e}}$, $\mathbf{f}$ and $\mathbf{e}$ are given in Appendix A.

The kinetic energy for the volume Ω can be given by

$$K = \frac{1}{2}\int_{\Omega} \rho \dot{u}_i^2 \mathrm{d}V \tag{5}$$

where ϱ is the mass density. Furthermore, the overhead "·" and "··" represent, respectively, the first- and second-time derivatives.

2.2 Basic equations

In this part, we focus on the basic kinematics equations for a Mindlin-type microplate continuum with uniform thickness h, as shown in Fig.1. A three-dimensional Cartesian coordinate system (x, y, z) is employed to describe the plate geometry, with its thickness direction along the z-axis and the middle plane ($z = 0$) lying on the x-y plane.

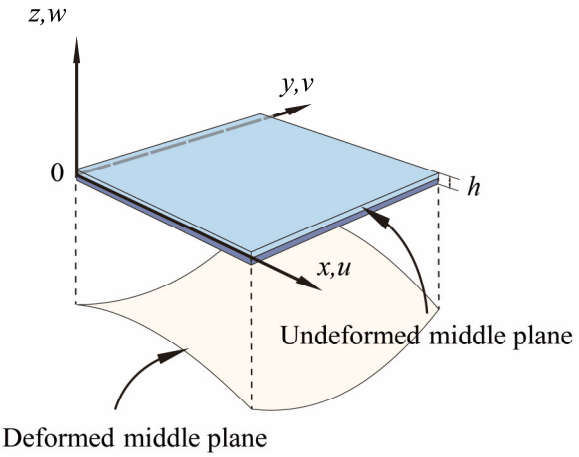

Fig.1 Geometry of the Mindlin-type microplate in Cartesian coordinates

Based on the classical geometry assumptions of Mindlin plate, the displacement field of the microplate can be described as ([21], Gao and Zhang 2016):

$$\begin{aligned} u(x,y,z,t) &= -z\phi_x(x,y,t), \\ v(x,y,z,t) &= -z\phi_y(x,y,t), \\ w(x,y,z,t) &= w(x,y,t), \end{aligned} \tag{6}$$

where $w(x, y, t)$ is the deflection of the middle plane. $\boxtimes_x(x, y, t)$ and $\boxtimes_y(x, y, t)$ are the rotation components of the middle plane shown in Fig.1 and defined by

$$\begin{aligned} \phi_x(x,y,t) &= \beta_x(x,y,t) + \frac{\partial w(x,y,t)}{\partial x}, \\ \phi_y(x,y,t) &= \beta_y(x,y,t) + \frac{\partial w(x,y,t)}{\partial y}, \end{aligned} \tag{7}$$

where $\beta_x(x, y, t)$ and $\beta_y(x, y, t)$ denote shear angles around x- and y-axis, respectively.

Substituting Eq. (6) into Eqs. (2) and (3) yields

$$\boldsymbol{\varepsilon} = \mathbf{S}_{\varepsilon}\hat{\boldsymbol{\varepsilon}}, \tag{8a}$$

$$\boldsymbol{\chi} = \mathbf{S}_{\chi}\hat{\boldsymbol{\chi}}. \tag{8b}$$

The electric potential φ in microplate can be assumed by [18,22]

$$\varphi(x,y,z,t) = z\varphi'(x,y,t)\ , \tag{9}$$

where φ' is the first-order electric potential.

From Eqs. (2) and (9), the electric field intensity vector $\mathbf{E}$ is expressed as

$$\mathbf{E} = -\mathbf{S}_E \hat{\mathbf{E}} . \tag{10}$$

Note that $\mathbf{S}_\varepsilon$, $\hat{\boldsymbol{\varepsilon}}$, $\mathbf{S}_\chi$, $\hat{\boldsymbol{\chi}}$, $\mathbf{S}_E$ and $\hat{\mathbf{E}}$ in Eqs. (8a, b) and (10) are listed in Appendix B.

2.3 Weak form

According to variational principle [18,22], based on Eqs. (1), (4), (5), (8a, b) and (10), the weak form of the current microplate can be summarized as follows:

$$\int_S \left[\delta\hat{\boldsymbol{\varepsilon}}^{\mathrm{T}} \hat{\mathbf{C}} \hat{\boldsymbol{\varepsilon}} + \delta\hat{\boldsymbol{\chi}}^{\mathrm{T}} \hat{\mathbf{f}}^{\mathrm{T}} \hat{\mathbf{E}} + \delta\hat{\mathbf{E}}^{\mathrm{T}} (\hat{\mathbf{f}}\hat{\boldsymbol{\chi}} - \hat{\mathbf{e}}\hat{\mathbf{E}}) \right] \mathrm{d}S = -\int_S \left(\delta\hat{\mathbf{u}}^{\mathrm{T}} \hat{\boldsymbol{\rho}}\, \ddot{\hat{\mathbf{u}}} \right) \mathrm{d}S \tag{11}$$

where S is the projected area of the corresponding microplate, dS is the area element, $\hat{\mathbf{u}} = \{w(x,y,t), \phi_x(x,y,t), \phi_y(x,y,t)\}^{\mathrm{T}}$ is the transformed displacement vector of the Mindlin plate, and $\hat{\boldsymbol{\rho}}$ is also provided in Appendix B. Besides, the generalized constitutive matrices $\hat{\mathbf{C}}$, $\hat{\mathbf{f}}$, $\hat{\mathbf{e}}$ are as follows:

$$\begin{aligned}
\hat{\mathbf{C}} &= \int_{-\frac{h}{2}}^{\frac{h}{2}} \mathbf{S}_\varepsilon^{\mathrm{T}} \mathbf{C}^{\mathbf{m}} \mathbf{S}_\varepsilon \mathrm{d}z, \\
\hat{\mathbf{f}} &= \int_{-\frac{h}{2}}^{\frac{h}{2}} \mathbf{S}_E^{\mathrm{T}} \mathbf{f} \mathbf{S}_\chi \mathrm{d}z, \\
\hat{\mathbf{e}} &= \int_{-\frac{h}{2}}^{\frac{h}{2}} \mathbf{S}_E^{\mathrm{T}} \mathbf{e} \mathbf{S}_E \mathrm{d}z,
\end{aligned} \tag{12}$$

where $\mathbf{C}^{\mathbf{m}}$ is the elastic stiffness matrix in Mindlin plate theory, and it is given in Appendix A.

Considering the time-harmonic displacements, Eq. (11) can be written as

$$\int_S \left[\delta\hat{\boldsymbol{\varepsilon}}^{\mathrm{T}} \hat{\mathbf{C}} \hat{\boldsymbol{\varepsilon}} + \delta\hat{\boldsymbol{\chi}}^{\mathrm{T}} \hat{\mathbf{f}}^{\mathrm{T}} \hat{\mathbf{E}} + \delta\hat{\mathbf{E}}^{\mathrm{T}} (\hat{\mathbf{f}}\hat{\boldsymbol{\chi}} - \hat{\mathbf{e}}\hat{\mathbf{E}}) \right] \mathrm{d}S - \omega^2 \int_S \left(\delta\hat{\mathbf{u}}^{\mathrm{T}} \hat{\boldsymbol{\rho}}\, \hat{\mathbf{u}} \right) \mathrm{d}S = 0 \tag{13}$$

where ω is angular frequency. Eq. (13) will be used to obtain the eigenfrequencies.

3. Finite element discretization

3.1 Implementation of triangular microplate

Meshing a microplate over the projected area $\boldsymbol{S}$ with three-node triangular elements as shown in Fig.2, where Γ_d and Γ_f are, respectively, displacement (also called essential) boundary conditions and force (also called natural) boundary conditions, $L_i (i = 1, 2, 3)$ refers to area coordinates.

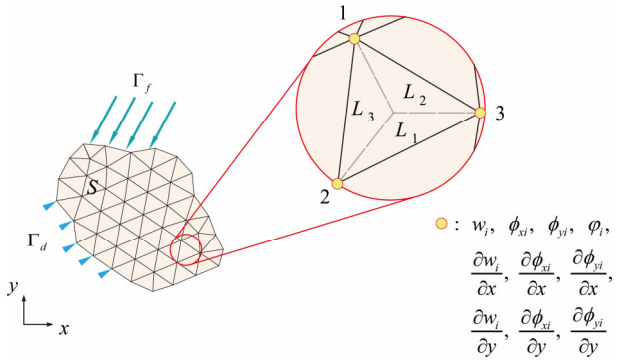

Fig.2 A microplate discretized by a 3-noded plate triangle with 30 DOFs

A three-node plate triangle with 30 DOFs shown in Fig.2 is implemented to solve the flexoelectric problem that is the coupling between polarization and strain gradients. For displacement field, the components of $\hat{\mathbf{u}}$ are approximated by

$$\begin{aligned} w &= \sum_i^3 N_i w_i + N_i^s \frac{\partial w_i}{\partial x} + N_i^t \frac{\partial w_i}{\partial y}, \\ \phi_x &= \sum_i^3 N_i \phi_{xi} + N_i^s \frac{\partial \phi_{xi}}{\partial x} + N_i^t \frac{\partial \phi_{xi}}{\partial y}, \\ \phi_y &= \sum_i^3 N_i \phi_{yi} + N_i^s \frac{\partial \phi_{yi}}{\partial x} + N_i^t \frac{\partial \phi_{yi}}{\partial y}, \end{aligned} \tag{14}$$

where the shape functions N_i, N_i^s and N_i^t are listed in Appendix C. Furthermore, the element nodal displacement vector can be expressed as

$$\mathbf{u}^e = \{w_1, \phi_{x1}, \phi_{y1}, \frac{\partial w_1}{\partial x}, \frac{\partial \phi_{x1}}{\partial x}, \frac{\partial \phi_{y1}}{\partial x}, \frac{\partial w_1}{\partial y}, \frac{\partial \phi_{x1}}{\partial y}, \frac{\partial \phi_{y1}}{\partial y}, \cdots\}_{1\times 27}^{\mathrm{T}}. \tag{15}$$

Substituting Eq. (15) into Eqs. (B.2) and (B.4), respectively, the generalized strain and curvature vectors are expressed by

$$\begin{aligned} \hat{\boldsymbol{\varepsilon}} &= \mathbf{B}_{\varepsilon} \mathbf{u}^e, \\ \hat{\boldsymbol{\chi}} &= \mathbf{B}_{\chi} \mathbf{u}^e. \end{aligned} \tag{16}$$

For electric field, the first-order electrical potential φ' is approximated by $\varphi' = \sum_{i=1}^{3} N_i^e \varphi_i'$, where the element nodal electrical potential vector is $\boldsymbol{\varphi}'^e = \{\varphi_1', \varphi_2', \varphi_3'\}^{\mathrm{T}}$, and the shape functions N_i^e are listed in Appendix C. The static electric field vector $\hat{\mathbf{E}}$ can be obtained as follows:

$$\hat{\mathbf{E}} = \mathbf{B}_E \boldsymbol{\varphi}'^e. \tag{17}$$

Note that $\mathbf{B}_{\varepsilon}$, $\mathbf{B}_{\chi}$, $\mathbf{B}_E$ are shown in Appendix C.

Substituting Eqs. (16) and (17) into Eq. (13), the element dynamic matrix equations can be written as

$$\begin{bmatrix} \mathbf{K}_{11} & \mathbf{K}_{12} \\ \mathbf{K}_{21} & \mathbf{K}_{22} \end{bmatrix} \begin{Bmatrix} \mathbf{u}^e \\ \boldsymbol{\varphi}'^e \end{Bmatrix} - \omega^2 \begin{bmatrix} \mathbf{M}_{11} & 0 \\ 0 & 0 \end{bmatrix} \begin{Bmatrix} \mathbf{u}^e \\ \boldsymbol{\varphi}'^e \end{Bmatrix} = 0, \tag{18}$$

where the components matrices $\mathbf{M}_{11}$, $\mathbf{K}_{11}$, $\mathbf{K}_{12}$, $\mathbf{K}_{21}$, and $\mathbf{K}_{22}$ are given in Appendix C.

3.2 Bloch-periodic boundary conditions

Based on Bloch's theorem, the displacement field of elastic wave propagation can be written in a harmonic function as

$$\mathbf{u}(\mathbf{r},\mathbf{k},t) = \mathbf{u}_k(\mathbf{r}) e^{\mathrm{i}\mathbf{k}\cdot\mathbf{r}} e^{\mathrm{i}\omega t} \ , \tag{19}$$

where $\mathbf{k}$ is the wavevector, $\mathbf{r}$ is the coordinate vector of the unit cell, $\mathbf{u}_k(\mathbf{r})$ is a periodic function consistent with the periodicity of the structure. To implement the Bloch boundary conditions, it is convenient to divide the unit cell boundary nodal variables into nine subsets by distinguishing the edges and corners. As shown in Fig. 3, we note therefore:

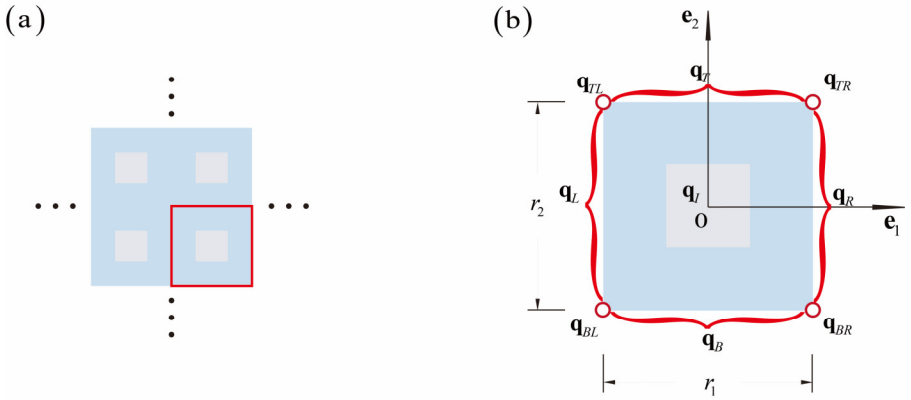

Fig.3 (a) Periodic 2D material, and (b) nine sets of the nodal variable [23] in the referenced unit cell (surrounded by a red border)

Nodal variables on the right and top boundaries $\mathbf{q}_R$ and $\mathbf{q}_T$ are related to those on the left and bottom boundaries $\mathbf{q}_L$ and $\mathbf{q}_B$, respectively. Therefore,

$$\begin{aligned} \mathbf{q}_R &= \lambda_1 \mathbf{q}_L, \\ \mathbf{q}_T &= \lambda_2 \mathbf{q}_B, \end{aligned} \tag{20}$$

where $\lambda_1 = e^{\mathrm{i}\mathbf{k}\cdot\mathbf{r}_1}$, $\lambda_2 = e^{\mathrm{i}\mathbf{k}\cdot\mathbf{r}_2}$, $\mathbf{r}_1$ and $\mathbf{r}_2$ are the relevant base vectors. Similarly, we use the following expressions to describe the kinematics of the corner nodes:

$$\begin{aligned} \mathbf{q}_{BR} &= \lambda_1 \mathbf{q}_{BL}, \\ \mathbf{q}_{TL} &= \lambda_2 \mathbf{q}_{BL}, \\ \mathbf{q}_{TR} &= \lambda_1 \lambda_2 \mathbf{q}_{BL}. \end{aligned} \tag{21}$$

These boundary conditions satisfy the Bloch theorem (Eq. (19)) and implement the periodic conditions on the free DOF vector $\mathbf{Q} = \{\mathbf{q}_I, \mathbf{q}_L, \mathbf{q}_R, \mathbf{q}_B, \mathbf{q}_T, \mathbf{q}_{BL}, \mathbf{q}_{BR}, \mathbf{q}_{TR}, \mathbf{q}_{TL}\}^{\mathrm{T}}$ with respect to the independent DOF vector $\hat{\mathbf{Q}} = \{\mathbf{q}_I, \mathbf{q}_L, \mathbf{q}_B, \mathbf{q}_{BL}\}^{\mathrm{T}}$. Therefore, the Bloch boundary conditions applied to the periodic unit cell can be expressed as:

$$\mathbf{Q} = \mathbf{P}\hat{\mathbf{Q}}\,, \tag{22}$$

where the transfer matrix $\mathbf{P}$ that defines the periodic conditions is given as:

$$\mathbf{P} = \begin{bmatrix} \mathbf{I} & 0 & 0 & 0 \\ 0 & \mathbf{I} & 0 & 0 \\ 0 & \lambda_1\mathbf{I} & 0 & 0 \\ 0 & 0 & \mathbf{I} & 0 \\ 0 & 0 & \lambda_2\mathbf{I} & 0 \\ 0 & 0 & 0 & \mathbf{I} \\ 0 & 0 & 0 & \lambda_1\mathbf{I} \\ 0 & 0 & 0 & \lambda_1\lambda_2\mathbf{I} \\ 0 & 0 & 0 & \lambda_2\mathbf{I} \end{bmatrix}.$$

Assembling the entire system and using Eq. (22), Eq. (18) can be further expressed as

$$(\mathbf{P}^{\mathrm{T}}\mathbf{K}\mathbf{P} - \omega^2\mathbf{P}^{\mathrm{T}}\mathbf{M}\mathbf{P})\hat{\mathbf{Q}} = 0\,. \tag{23}$$

This is the final form of the unit cell governing equation of free vibration with the account for Bloch boundary conditions. For a given wave vector $\mathbf{k}$, the corresponding eigen-frequencies ω can be obtained by performing modal analysis based on Eq. (23). The real-valued wave vector $\mathbf{k}$ that is not in the range of ω will be identified as bandgaps.

4. Numerical results

Flexoelectric effect describes the coupling between non-uniform deformation and the induced electrical responses. It is a common phenomenon in all dielectric materials, however, its observation is most obvious in centrosymmetric dielectric materials [7-9]. In this section, we consider centrosymmetric cubic materials in the *O* class of crystals and investigate their bandgap properties. The material composition of the unit cell is distinguished between Phases I and II, based on PbS and epoxy, respectively, whose properties are given in Table 1.

Table 1 Material parameters of PbS and epoxy ([24-28])

Material	PbS	Epoxy
$\rho\ (\mathrm{kg/m^3})$	7600	1180
c_{11} (GPa)	127	4.889
c_{12} (GPa)	29.8	2.408
c_{44} (GPa)	24.8	1.241
$\dot{\mathrm{q}}_{11}\ (10^{-9}\mathrm{C}^2/(\mathrm{Nm}^2))$	1.567	0.0426
$g_1\ (10^{-8}\mathrm{C/m})$	0.75	3

4.1 Validation

To validate the proposed numerical framework, let us consider a square unit cell composed of centrosymmetric dielectric materials shown in Fig. 4a. Then, the edges Γ-X-M-Γ in Fig. 4b

refer to the boundary of the irreducible first Brillouin zone in the reciprocal space, considered for band gap calculations [2]. The unit cell thickness $h = 5$ μm, the unit length $L = 20h$ and the volume fraction of Phase I $V_{\mathrm{I}} = 16\%$ (i.e., $c = 0.4L$) are considered in this section.

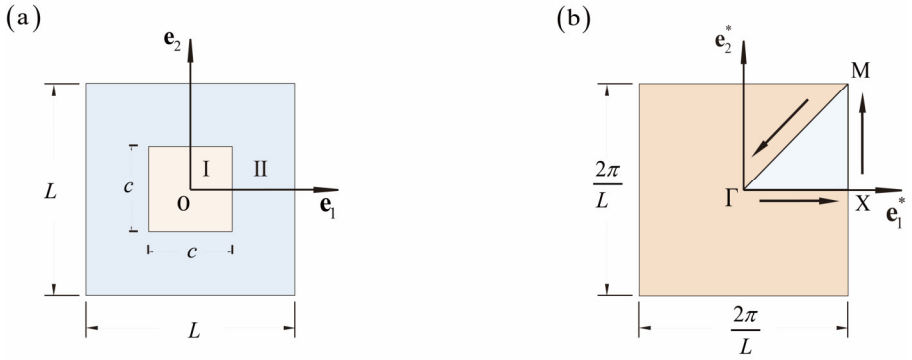

Fig. 4 (a) The geometry of the unit cell structure (b) Representation of the irreducible first Brillouin zone in the reciprocal space

Based on this unit cell, the results of the proposed flexoelectric model using two mesh densities depicted in Fig.5 are considered to compare with predictions by plane wave expansion method (PWE) involving flexoelectric effect. Equations implemented in this example for PWE calculations are given in Appendix D. Plane wave expansion of order 25 is used to ensure the accuracy of the result. The obtained band diagrams are plotted in Fig. 6.

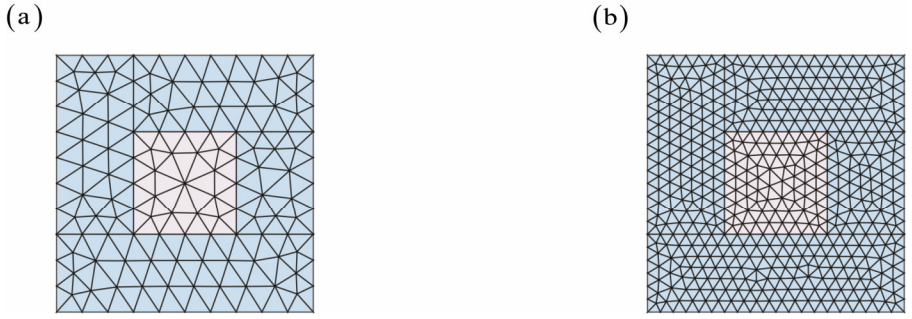

Fig. 5 Two mesh refinements based on triangular elements: (a) 10 × 10, (b) 20 × 20

From Fig. 6, it is observed that the result of the proposed flexoelectric model approaches the PWE result with increased mesh refinement, as expected. Bandgap computed using the 20 × 20 mesh perfectly agrees with the PWE result to the third decimal, suggesting that the 20 × 20 mesh refinement is sufficient for obtaining converged solution.

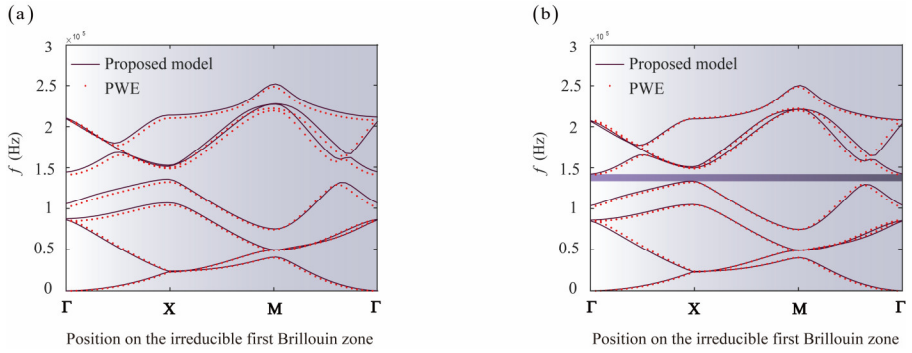

Fig. 6 Compared to PWE, the band structures obtained by the proposed model with (a) meshing density of 10×10 (b) meshing density of 20×20

4.2 Size effect of the flexoelectric model in bandgap analysis

In this section, we adopt the unit cell microstructure of Section 4.1 and investigate the size dependence of bandgap properties using the flexoelectric model. Therefore, we perform a series of bandgap calculations based on a range of problem sizes for which size effects will gradually emerge. The calculations are carried out using both the proposed flexoelectric model and classical elasticity model. Results from the two models are expected to diverge with the emergence of size effects since only behaviors of flexoelectricity are size-dependent.

The problem size we have considered varies first within submicron range with the unit cell thickness $h = 0.2 \sim 0.9$ μm, then with $h = 20 \sim 90$ μm. The frequency range of the first bandgap is plotted as function of h, for both the flexoelectric and classical elasticity models, in Fig.7.

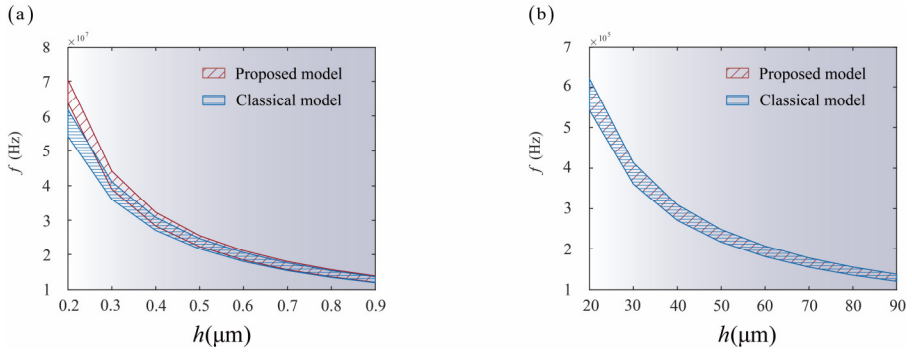

Fig. 7 Bandgap frequency ranges corresponding to different plate thickness: (a) the range of thickness $h = 0.2 \sim 0.9$ μm (b) the range of thickness $h = 20 \sim 90$ μm

Significant difference can be noticed on the bandgap frequency range calculated with the flexoelectric and classical elasticity models according to Fig.7(a), especially on small problem sizes with h approaching 0.2 μm. Distinct bandgaps can be observed at $h = 0.2$ μm, with the frequency ranges [63.66 MHz, 70.43 MHz], and [54.12 MHz, 61.73 MHz], obtained by flexoelectric and classical elasticity models, respectively. This difference can be explained by the fact that only the effect of flexoelectricity is size-dependent. Therefore, size effect which is most significant on sub-micron problems has been accounted for only by the flexoelectric model. For the same reason, with larger problem sizes, the two models gradually converge with h approaching 0.9 μm. Significance of size effects becomes negligible with h going beyond the micron meter level, thus in Fig.7(b) which depicts the cases with $h = 20 \sim 90$ μm, the flexoelectric and classical elasticity models completely agree with each other.

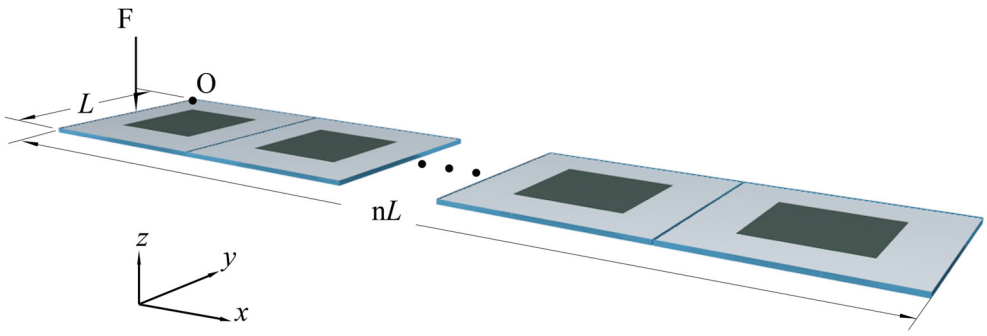

Fig.8 A spatial periodic composite microplate structure composed of n unit cells

To study the effectiveness of the bandgap calculation, we further perform dynamic response analysis in time domain using Newmark implicit integration based on a real scale composite microplate structure. The structure is composed of n unit cells periodically arranged along x axis, as shown in Fig. (8). Application of Newmark integration allows calculating the dynamic response of the structure following an input excitation prescribed as function of time. For reasons of convenience, we consider n=3 and set point O as the coordinate origin (i.e., x=0, y=0). A harmonic excitation signal F=F_0sin(ωt) is prescribed at the point (x, y) = (0, -L/2), where F_0=1x10^{-7} N. Other boundary conditions involve fixed constraints at the points (x, y) = (3L, 0) and (x, y) = (3L, -L). Measurement of the dynamic response is performed at the point (x, y) = (3L, -L/2).

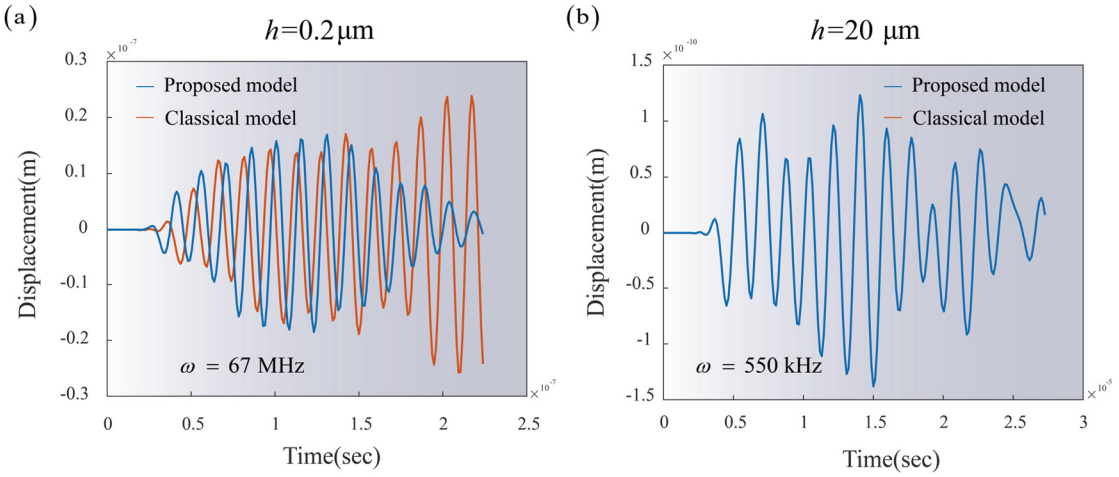

Fig.9 Dynamic response of proposed model and classical model in Time Domain: (a) thickness h = 0.2 μm and the frequency of harmonic excitation signal ω=67 MHz; (b) thickness h = 20 μm and the frequency of harmonic excitation signal ω=550 kHz;

To make meaningful comparison that confronts bandgap predictions (Fig.7) with dynamic response simulations, we prescribe a harmonic excitation to the composite microplate and compare the dynamic responses by considering both the flexoelectric and classical elasticity models. Specifically, we consider a problem configuration with h = 0.2 μm, which has shown significant size effect as reported in Fig.7(a). We then apply an excitation signal with ω=67 MHz, which belongs to the bandgap predicted by the flexoelectric model, but not by the classical

elasticity model. Comparison made on the dynamic response in time domain using both models (see Fig.9(a)) leads to the following observation: since the input excitation (ω=67 MHz) lies in the bandgap of the flexoelectric model only, we observe significant attenuation on the dynamic response of the flexoelectric model, whereas the classical elasticity model gives amplified response, which is normal since the prescribed excitation lies beyond its bandgap. Similarly, we perform further tests by considering another configuration with $h = 20$ μm, which according to Fig.7(b) does not demonstrate visible size effect. We then prescribe on the microplate an input excitation of frequency ω=550 kHz, which belongs to the bandgap of both the flexoelectric and classical elasticity models. This times, we observed concordant dynamic responses, which both attenuate with time. This observation complies with the theoretical prediction, since input waves within the bandgap get attenuated during propagation and, since the problem size does not involve microstructure effect, the flexoelectric and classical theory models present equivalent dynamic behaviors.

4.3 Effect of volume fraction on bandgaps

In Section 4.2, we investigated the size dependence of flexoelectric effect in bandgap calculations and proposed a dynamic response simulation in time domain to confirm the effectiveness of our approach. In this section, we continue with the same unit cell microstructure and further study the influence on the bandgap behaviors by the volume fraction of the inclusion. We recall the dimension of the unit cell given by $L \times L$, with $L = 20h$. Since the inclusion (Phase I) is defined by variable volume with the volume fraction denoted by $V_I = c^2/L^2$, we prescribe a series of bandgap calculations by considering V_I that evolves on the range $V_I = 0.05 \sim 0.5$. Additionally, we perform two groups of tests by considering distinct problem sizes with the unit cell thickness $h = 0.2$ μm and 20 μm, respectively. Therefore, significant size-dependent flexoelectric effect can be expected on the submicron $h = 0.2$ μm case.

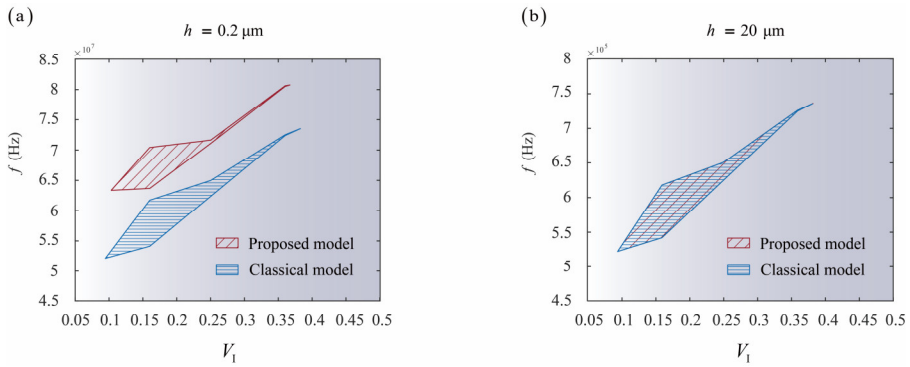

Fig. 10 The bandgaps corresponding to different volume fraction V_I:(a) $h = 0.2$ μm (b) $h = 20$ μm

We present in Fig. 10 evolution of the first bandgap calculated with respect to the inclusion volume fraction for both problem sizes. The result compares the proposed flexoelectric model with the classical elasticity model. Therefore, we notice similar size effects by comparing Fig. 10 (a) and (b) where size-dependent flexoelectric effect is only observed on the submicron problem (Fig. 10 (a)), which is coherent with the conclusion of Section 4.2 (Fig. 7). In addition, the following observations can be drawn based on the analysis of Fig. 10 (a) and (b): first, the inclusion volume fraction has significant influence on the structure's bandgap property. With $V_{\mathrm{I}} < 0.1$ or $V_{\mathrm{I}} > 0.4$, the bi-phase microstructure does not present visible bandgap at all. Then, both the range and position of the bandgap are function of the inclusion volume fraction V_{I}. Consequently, results depicted in Fig. 10 (a) and (b) can be used to assist the design of the bi-phase microstructure, leading to tunable bandgap behaviors with the account for size-dependent flexoelectric effects.

4.4 Bandgap of an anti-chiral metastructure with flexoelectric effects

In the previous examples, we confirmed the accuracy of the proposed numerical model via comparison with PWE solutions. The cases we investigated only involve basic square geometries due to the limitations of the PWE method, which requires building shape functions specific to each model and is therefore ineffective in treating complex geometries. To illustrate the versatility and capacity of the proposed numerical model in dealing with complex microstructures, we investigate in this example bandgap properties of an anti-tetrachiral metastructure ([29,30]). As shown in Fig.11(a), the anti-tetrachiral unit cell is composed of circular nodes connected by straight ligaments that are tangent to them. The circular nodes are of radius r and the ligaments are of length a. The structure wall thickness is d with depth h. The bi-phase material consists of PbS for Phase I and Epoxy for Phase II, whose properties are given in Table 1. The unit cell geometry parameters are defined with respect to h as: $2a = 20h$, d $= 0.5h$ and $r = 2.5h$. Bandgap calculation is performed by considering the boundary of the irreducible first Brillouin zone (Fig. 11(b)), indicated by the path Γ-X-M-N-M and defined in the reciprocal space of the unit cell.

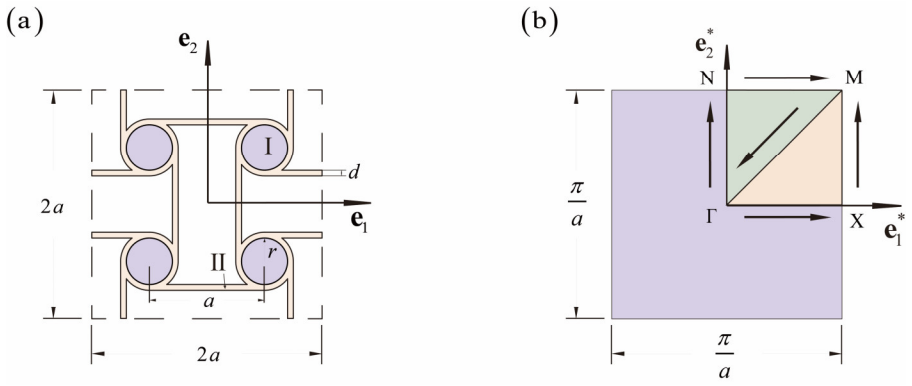

Fig. 11 (a) The unit cell of the anti-tetrachiral metastructure ([30]) (b) Irreducible first Brillouin zone in the reciprocal space.

As shown in Figs.12(a-c), three mesh densities containing 1140, 1592 and 3248 elements, respectively, have been considered to evaluate the mesh convergence properties of the proposed model. The obtained band diagrams are reported in Fig.12(d-f), where we can observe good convergence of the band structure with respect to mesh refinement. Taking the case with $h = 0.2$ μm as an example, the second bandgap frequency range obtained with the three cases are [48.75 MHz, 130.70 MHz], [47.62 MHz, 127.62 MHz] and [46.28 MHz, 124.83 MHz], for the coarse, medium and fine mesh refinements, respectively. We observe therefore stabilized result that begins with the medium mesh. Besides, the shape of the band frequency curves is equivalent for the three cases, suggesting negligible mesh dependence. Hence, the test cases lead to confirmed stability and mesh convergence of the proposed model. In the following, the fine mesh configuration is adopted to study the property of size dependence due to flexoelectric effects.

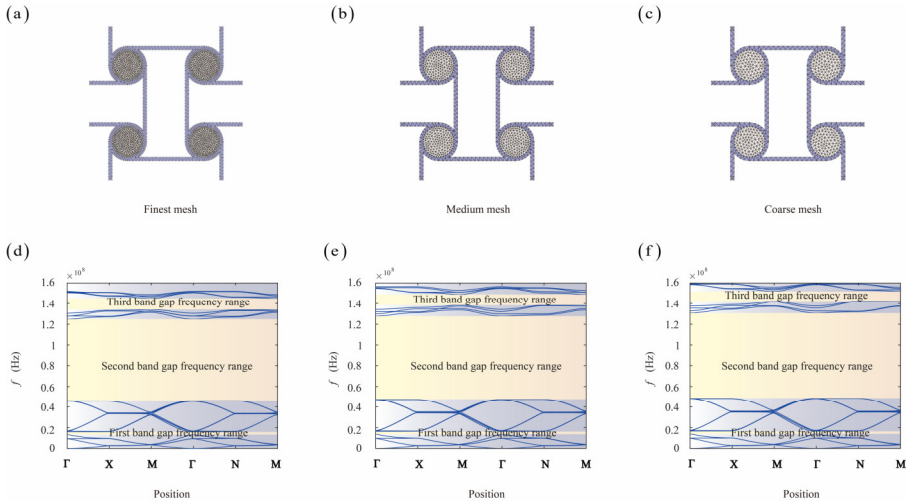

Fig. 12 The three mesh refinements, with fine mesh (a), medium mesh (b), and coarse mesh (c). The bandgap diagrams calculated using the fine mesh (d), medium mesh (e) and coarse mesh (f).

Based on the fine mesh configuration which presents confirmed mesh convergence, we investigate the flexoelectric effect via the induced size dependence on bandgap properties. Therefore, we prescribe two groups of tests with different problem sizes. The first group consists of cases with thickness ranging from 0.2 μm to 0.9 μm, and the second group consists of significantly larger problems, with the thickness ranging from 20 μm to 90 μm. For both situations, we compare the size of the first bandgap by considering models with and without flexoelectric effects, and we report the results in Fig.13.

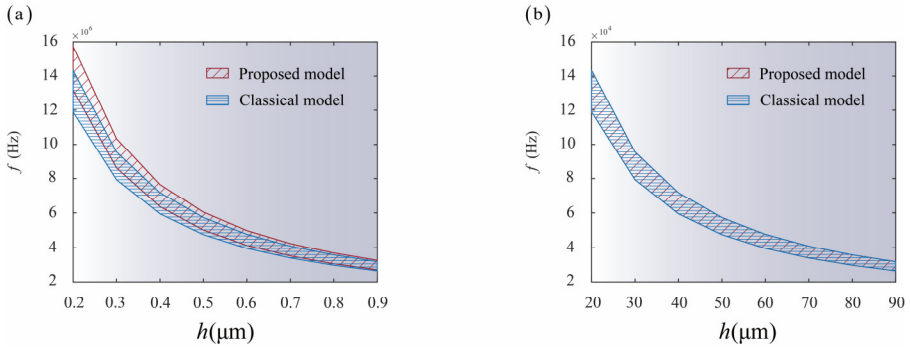

Fig. 13 First bandgap frequency range as function of the plate thickness: (a) cases in the thickness range $h = 0.2 \sim 0.9$ μm, (b) cases in the thickness range $h = 20 \sim 90$ μm.

We observe in Fig.13(b) perfect coincidence between the flexoelectric model and the classical model, which indicates negligible flexoelectric effect on larger problem sizes. This is normal since bandgap properties are not size-dependent on macro scale problems. On the contrary, bandgap results depicted in Fig.13(a) do not coincide. The account for flexoelectric effect leads to significant size dependence of the bandgap property on micro scale problems. This further suggests that the size-dependent flexoelectricity effect is mostly visible on the submicron scale, which agrees with the findings in Section 4.2

5. Summary

In this work, a high-order finite element model is proposed to predict elastic wave bandgaps of composite microplates involving flexoelectric effects. A three-node triangle plate element with 30 DOFs is implemented to accommodate the formulation of curvature-based flexoelectric theory, and we applied Bloch's theorem for the bandgap calculation based on the composite's periodic unit cell. In terms of numerical implementation of the flexoelectricity theory, our model has been validated via comparison with analytical PWE method and its application on an anti-tetrachiral metastructure has proved its adaptability on problems involving complex geometries. Then, regarding the physical interpretation of the simulations, our investigations revealed that the size-dependent flexoelectric effect cannot be neglected for problems of submicron level, whereas it does not present significance on structures larger than the micrometer level. Future extensions of the work should include investigation of flexoelectric effects on soft dielectric materials, and integration of other size-dependences such as surface effects etc. [31-37].

References

[1] Hsu J C, Wu T T. Efficient formulation for band-structure calculations of two-dimensional phononic-crystal plates[J]. Physical review B, 2006, 74(14): 144303.

[2] Kushwaha M S, Halevi P, Dobrzynski L, et al. Acoustic band structure of periodic elastic composites[J]. Physical review letters, 1993, 71(13): 2022.

[3] Sigalas M M, Economou E N. Elastic waves in plates with periodically placed inclusions[J]. Journal of Applied Physics, 1994, 75(6): 2845-2850.

[4] Baravelli E, Ruzzene M. Internally resonating lattices for bandgap generation and low-frequency vibration control[J]. Journal of Sound and Vibration, 2013, 332(25): 6562-6579.

[5] Jo S H, Yoon H, Shin Y C, et al. Elastic wave localization and harvesting using double defect modes of a phononic crystal[J]. Journal of Applied Physics, 2020, 127(16): 164901.

[6] Laude V, Laforge N, Chollet F, et al. Guided waves along a domain wall of a water wave crystal[C]//Workshop on Seismic Metamaterials: From Optics to Geophysics. 2019.

[7] Yudin P V, Tagantsev A K. Fundamentals of flexoelectricity in solids[J]. Nanotechnology, 2013, 24(43): 432001.

[8] Zubko P, Catalan G, Tagantsev A K. Flexoelectric effect in solids[J]. Annual Review of Materials Research, 2013, 43: 387-421.

[9] Nguyen T D, Mao S, Yeh Y W, et al. Nanoscale flexoelectricity[J]. Advanced Materials, 2013, 25(7): 946-974.

[10] Lam D C C, Yang F, Chong A C M, et al. Experiments and theory in strain gradient elasticity[J]. Journal of the Mechanics and Physics of Solids, 2003, 51(8): 1477-1508.

[11] Deng Q, Lv S, Li Z, et al. The impact of flexoelectricity on materials, devices, and physics[J]. Journal of Applied Physics, 2020, 128(8): 080902.

[12] Yvonnet J, Liu L P. A numerical framework for modeling flexoelectricity and Maxwell stress in soft dielectrics at finite strains[J]. Computer Methods in Applied Mechanics and Engineering, 2017, 313: 450-482.

[13] Deng F, Deng Q, Yu W, et al. Mixed finite elements for flexoelectric solids[J]. Journal of Applied Mechanics, 2017, 84(8).

[14] Deng F, Deng Q, Shen S. A three-dimensional mixed finite element for flexoelectricity[J]. Journal of Applied Mechanics, 2018, 85(3).

[15] Liu C, Hu S, Shen S. Effect of flexoelectricity on band structures of one-dimensional phononic crystals[J]. Journal of Applied Mechanics, 2014, 81(5).

[16] Yang W, Hu T, Liang X, et al. On band structures of layered phononic crystals with flexoelectricity[J]. Archive of Applied Mechanics, 2018, 88(5): 629-644.

[17] Qu Y L, Zhang G Y, Fan Y M, et al. A non-classical theory of elastic dielectrics incorporating couple stress and quadrupole effects: part I–reconsideration of curvature-

based flexoelectricity theory[J]. Mathematics and Mechanics of Solids, 2021, 26(11): 1647-1659.

[18] Zhang G Y, He Z Z, Gao X L, et al. Band gaps in a periodic electro-elastic composite beam structure incorporating microstructure and flexoelectric effects[J]. Archive of Applied Mechanics, 2022: 1-16.

[19] Argyris J H, Fried I, Scharpf D W. The TUBA family of plate elements for the matrix displacement method[J]. The Aeronautical Journal, 1968, 72(692): 701-709.

[20] Xia Z X, Zhang G Y, Cong Y, et al. A non-classical couple stress based Mindlin plate finite element framework for tuning band gaps of periodic composite micro plates[J]. Journal of Sound and Vibration, 2022, 529: 116889.

[21] Gao X L, Zhang G Y. A non-classical Mindlin plate model incorporating microstructure, surface energy and foundation effects[J]. Proceedings of the Royal Society A: Mathematical, Physical and Engineering Sciences, 2016, 472(2191): 20160275.

[22] Zhang G, Qu Y, Guo Z, et al. Magnetically induced electric potential in first-order composite beams incorporating couple stress and its flexoelectric effects[J]. Acta Mechanica Sinica, 2021, 37(10): 1509-1519.

[23] Krattiger D, Hussein M I. Generalized Bloch mode synthesis for accelerated calculation of elastic band structures[J]. Journal of Computational Physics, 2018, 357: 183-205.

[24] Lam D C C, Yang F, Chong A C M, et al. Experiments and theory in strain gradient elasticity[J]. Journal of the Mechanics and Physics of Solids, 2003, 51(8): 1477-1508.

[25] Park S K, Gao X L. Bernoulli–Euler beam model based on a modified couple stress theory[J]. Journal of Micromechanics and Microengineering, 2006, 16(11): 2355.

[26] Anderson P M, Hirth J P, Lothe J. Theory of dislocations[M]. Cambridge University Press, 2017. pp. 837.

[27] Nag B R. Empirical formula for the dielectric constant of cubic semiconductors[J]. Applied physics letters, 1994, 65(15): 1938-1939.

[28] Qu Y L, Li P, Zhang G Y, et al. A microstructure-dependent anisotropic magneto-electro-elastic Mindlin plate model based on an extended modified couple stress theory[J]. Acta Mechanica, 2020, 231(10): 4323-4350.

[29] Qi D, Yu H, Hu W, et al. Bandgap and wave attenuation mechanisms of innovative reentrant and anti-chiral hybrid auxetic metastructure[J]. Extreme Mechanics Letters, 2019, 28: 58-68.

[30] Wu W, Hu W, Qian G, et al. Mechanical design and multifunctional applications of chiral mechanical metamaterials: A review[J]. Materials & Design, 2019, 180: 107950.

[31] Deng Q, Liu L, Sharma P. Flexoelectricity in soft materials and biological membranes[J]. Journal of the Mechanics and Physics of Solids, 2014, 62: 209-227.

[32] Chen Y, Wu B, Su Y, et al. Effects of strain stiffening and electrostriction on tunable

elastic waves in compressible dielectric elastomer laminates[J]. International Journal of Mechanical Sciences, 2020, 176: 105572.

[33] Wu B, Zhou W, Bao R, et al. Tuning elastic waves in soft phononic crystal cylinders via large deformation and electromechanical coupling[J]. Journal of Applied Mechanics, 2018, 85(3).

[34] Wu B, Chen W, Zhang C. On free vibration of piezoelectric nanospheres with surface effect[J]. Mechanics of Advanced Materials and Structures, 2018, 25(13): 1101-1114.

[35] Wu B, Zhang C, Chen W, et al. Surface effects on anti-plane shear waves propagating in magneto-electro-elastic nanoplates[J]. Smart Materials and Structures, 2015, 24(9): 095017.

[36] Wang K F, Wang B L. A finite element model for the bending and vibration of nanoscale plates with surface effect[J]. Finite Elements in Analysis and Design, 2013, 74: 22-29.

[37] Liang X, Hu S, Shen S. Effects of surface and flexoelectricity on a piezoelectric nanobeam[J]. Smart materials and structures, 2014, 23(3): 035020.

Appendix A

Cubic material -O class:

Elastic stiffness matrices

$$\mathbf{C^e} = \begin{bmatrix} c_{11} & c_{12} & c_{12} & 0 & 0 & 0 \\ c_{12} & c_{11} & c_{12} & 0 & 0 & 0 \\ c_{12} & c_{12} & c_{11} & 0 & 0 & 0 \\ 0 & 0 & 0 & c_{44} & 0 & 0 \\ 0 & 0 & 0 & 0 & c_{44} & 0 \\ 0 & 0 & 0 & 0 & 0 & c_{44} \end{bmatrix} \tag{A.1}$$

$$\mathbf{C^m} = \begin{bmatrix} c_{11} - \frac{(c_{12})^2}{c_{11}} & c_{12} - \frac{(c_{12})^2}{c_{11}} & 0 & 0 & 0 \\ c_{12} - \frac{(c_{12})^2}{c_{11}} & c_{11} - \frac{(c_{12})^2}{c_{11}} & 0 & 0 & 0 \\ 0 & 0 & c_{44} & 0 & 0 \\ 0 & 0 & 0 & k_{11}c_{44} & 0 \\ 0 & 0 & 0 & 0 & k_{22}c_{44} \end{bmatrix} \tag{A.2}$$

where k_{11} and k_{22} are in-plane shear correction parameters, and they are both 5/6.

Flexoelectric coefficient matrix

$$\mathbf{f} = \begin{bmatrix} 0 & 0 & 0 & 0 & 0 & g_1 & 0 & g_1 & 0 \\ 0 & 0 & g_1 & 0 & 0 & 0 & g_1 & 0 & 0 \\ 0 & g_1 & 0 & g_1 & 0 & 0 & 0 & 0 & 0 \end{bmatrix} \tag{A.3}$$

Dielectric matrix

$$\mathbf{e} = \begin{bmatrix} \grave{\alpha}_1 & 0 & 0 \\ 0 & \grave{\alpha}_1 & 0 \\ 0 & 0 & \grave{\alpha}_1 \end{bmatrix} \tag{A.4}$$

Appendix B

The expressions of $\mathbf{S}_\varepsilon, \hat{\boldsymbol{\varepsilon}}, \mathbf{S}_\chi, \hat{\boldsymbol{\chi}}$ *and* $\hat{\boldsymbol{\rho}}$:

$$\mathbf{S}_\varepsilon = \begin{bmatrix} -z & 0 & 0 & 0 & 0 \\ 0 & -z & 0 & 0 & 0 \\ 0 & 0 & -z & 0 & 0 \\ 0 & 0 & 0 & 1 & 0 \\ 0 & 0 & 0 & 0 & 1 \end{bmatrix}, \tag{B.1}$$

$$\hat{\boldsymbol{\varepsilon}} = \begin{Bmatrix} \hat{\varepsilon}_x \\ \hat{\varepsilon}_y \\ \hat{\gamma}_{xy} \\ \hat{\gamma}_{xz} \\ \hat{\gamma}_{yz} \end{Bmatrix} = \begin{Bmatrix} \dfrac{\partial \phi_x}{\partial x} \\ \dfrac{\partial \phi_y}{\partial y} \\ \dfrac{\partial \phi_x}{\partial y} + \dfrac{\partial \phi_y}{\partial x} \\ -\phi_x + \dfrac{\partial w}{\partial x} \\ -\phi_y + \dfrac{\partial w}{\partial y} \end{Bmatrix}, \tag{B.2}$$

$$\mathbf{S}_z = \frac{1}{2} \begin{bmatrix} 1 & 0 & 0 & 0 & 0 & 0 & 0 & 0 & 0 \\ 0 & 1 & 0 & 0 & 0 & 0 & 0 & 0 & 0 \\ 0 & 0 & 1 & 0 & 0 & 0 & 0 & 0 & 0 \\ 0 & 0 & 0 & 1 & 0 & 0 & 0 & 0 & 0 \\ 0 & 0 & 0 & 0 & 1 & 0 & 0 & 0 & 0 \\ 0 & 0 & 0 & 0 & 0 & 1 & 0 & 0 & 0 \\ 0 & 0 & 0 & 0 & 0 & 0 & z & 0 & 0 \\ 0 & 0 & 0 & 0 & 0 & 0 & 0 & z & 0 \\ 0 & 0 & 0 & 0 & 0 & 0 & 0 & 0 & 1 \end{bmatrix}, \tag{B.3}$$

$$\hat{\boldsymbol{\chi}} = \begin{Bmatrix} \hat{\chi}_{xx} \\ \hat{\chi}_{xy} \\ \hat{\chi}_{xz} \\ \hat{\chi}_{yx} \\ \hat{\chi}_{yy} \\ \hat{\chi}_{yz} \\ \hat{\chi}_{zx} \\ \hat{\chi}_{zy} \\ \hat{\chi}_{zz} \end{Bmatrix} = \begin{bmatrix} \dfrac{\partial^2 w}{\partial x \partial y} + \dfrac{\partial \phi_y}{\partial x} \\ \dfrac{\partial^2 w}{\partial y^2} + \dfrac{\partial \phi_y}{\partial y} \\ 0 \\ -\dfrac{\partial^2 w}{\partial x^2} - \dfrac{\partial \phi_x}{\partial x} \\ -\dfrac{\partial^2 w}{\partial x \partial y} - \dfrac{\partial \phi_x}{\partial y} \\ 0 \\ -\dfrac{\partial^2 \phi_y}{\partial x^2} + \dfrac{\partial^2 \phi_x}{\partial x \partial y} \\ -\dfrac{\partial^2 \phi_y}{\partial x \partial y} + \dfrac{\partial^2 \phi_x}{\partial y^2} \\ -\dfrac{\partial \phi_y}{\partial x} + \dfrac{\partial \phi_x}{\partial y} \end{bmatrix}, \tag{B.4}$$

$$\mathbf{S}_{\mathrm{E}} = \begin{bmatrix} z & 0 & 0 \\ 0 & z & 0 \\ 0 & 0 & 1 \end{bmatrix}, \tag{B.5}$$

$$\hat{\mathbf{E}} = \begin{bmatrix} \hat{E}_x \\ \hat{E}_y \\ \hat{E}_z \end{bmatrix} = \begin{Bmatrix} \dfrac{\partial \varphi'}{\partial x} \\ \dfrac{\partial \varphi'}{\partial y} \\ \varphi' \end{Bmatrix}, \tag{B.6}$$

$$\hat{\boldsymbol{\rho}} = \begin{bmatrix} \rho h & 0 & 0 \\ 0 & \dfrac{\rho h^3}{12} & 0 \\ 0 & 0 & \dfrac{\rho h^3}{12} \end{bmatrix}. \tag{B.7}$$

Appendix C

The components of mass matrix and stiffness matrix:

$$\begin{aligned}
\mathbf{K}_{11} &= \int_S \mathbf{B}_\varepsilon^{\mathrm{T}} \hat{\mathbf{C}} \mathbf{B}_\varepsilon \mathrm{d}S \\
\mathbf{K}_{12} &= \int_S \mathbf{B}_\chi^{\mathrm{T}} \hat{\mathbf{f}}^{\mathrm{T}} \mathbf{B}_E \mathrm{d}S \\
\mathbf{K}_{21} &= \int_S -\mathbf{B}_E^{\mathrm{T}} \hat{\mathbf{f}} \mathbf{B}_\chi \mathrm{d}S \\
\mathbf{K}_{22} &= \int_S \mathbf{B}_E^{\mathrm{T}} \hat{\mathbf{e}} \mathbf{B}_E \mathrm{d}S \\
\mathbf{M}_{11} &= \int_S \mathbf{N}^{\mathrm{T}} \hat{\boldsymbol{\rho}} \mathbf{N} \mathrm{d}S
\end{aligned} \tag{C.1}$$

where the corresponding strain-displacement matrixes $\mathbf{B}_\varepsilon$, $\mathbf{B}_\chi$ and $\mathbf{B}_E$ are expressed as:

$$\mathbf{B}_\varepsilon = \begin{bmatrix} 0 & \dfrac{\partial}{\partial x} & 0 \\ 0 & 0 & \dfrac{\partial}{\partial y} \\ 0 & \dfrac{\partial}{\partial y} & \dfrac{\partial}{\partial x} \\ \dfrac{\partial}{\partial x} & -1 & 0 \\ \dfrac{\partial}{\partial y} & 0 & -1 \end{bmatrix} \mathbf{N} \tag{C.2}$$

$$\mathbf{B}_\chi = \begin{bmatrix} \dfrac{\partial^2}{\partial x \partial y} & 0 & \dfrac{\partial}{\partial x} \\ \dfrac{\partial^2}{\partial y^2} & 0 & \dfrac{\partial}{\partial y} \\ 0 & 0 & 0 \\ -\dfrac{\partial^2}{\partial x^2} & -\dfrac{\partial}{\partial x} & 0 \\ -\dfrac{\partial^2}{\partial x \partial y} & -\dfrac{\partial}{\partial y} & 0 \\ 0 & 0 & 0 \\ 0 & \dfrac{\partial^2}{\partial x \partial y} & -\dfrac{\partial^2}{\partial x^2} \\ 0 & \dfrac{\partial^2}{\partial y^2} & -\dfrac{\partial^2}{\partial x \partial y} \\ 0 & \dfrac{\partial}{\partial y} & -\dfrac{\partial}{\partial x} \end{bmatrix} \mathbf{N} \tag{C.3}$$

$$\mathbf{B}_E = \begin{bmatrix} \dfrac{\partial}{\partial x} \\ \dfrac{\partial}{\partial y} \\ 1 \end{bmatrix} \mathbf{N}^e \tag{C.4}$$

with the shape function matrix $\mathbf{N}$ and $\mathbf{N}^e$:

$$\mathbf{N}=\begin{bmatrix} N_1 & 0 & 0 & N_1^s & 0 & 0 & N_1^t & 0 & 0 & \cdots \\ 0 & N_1 & 0 & 0 & N_1^s & 0 & 0 & N_1^t & 0 & \cdots \\ 0 & 0 & N_1 & 0 & 0 & N_1^s & 0 & 0 & N_1^t & \cdots \end{bmatrix}_{3\times 27} \tag{C.5}$$

$$\mathbf{N}^e=\begin{bmatrix} N_1^e & N_2^e & N_3^e \end{bmatrix} \tag{C.6}$$

where

$$\begin{aligned} N_i &= L_i + L_i^2 L_j + L_i^2 L_k - L_i L_j^2 - L_i L_k^2, \\ N_i^s &= L_i^2 (b_j L_k - b_k L_j) + \frac{1}{2}(b_j - b_k) L_1 L_2 L_3, \\ N_i^t &= L_i^2 (c_j L_k - c_k L_j) + \frac{1}{2}(c_j - c_k) L_1 L_2 L_3, \\ N_1^e &= L_1, N_2^e = L_2, N_3^e = L_3, \end{aligned} \tag{C.6}$$

and $b_j = y_j - y_k$, $c_j = x_k - x_j$, L_i refers to area coordinates shown in Fig.2, with i, j, k are cyclic permutation indices.

Appendix D

The motion balance equations of the proposed curvature-based flexoelectricity Mindlin microplate are as follows:

$$\begin{aligned} \frac{\partial N_{xz}}{\partial x}+\frac{\partial N_{yz}}{\partial y}-\frac{1}{2}\frac{\partial^2\left(Y_{xx}-Y_{yy}\right)}{\partial x\partial y}+\frac{1}{2}\frac{\partial^2 Y_{yx}}{\partial x^2}-\frac{1}{2}\frac{\partial^2 Y_{xy}}{\partial y^2} &= m_0\frac{\partial^2 w}{\partial t^2}, \\ N_{xz}-\frac{\partial M_{xx}}{\partial x}-\frac{\partial M_{xy}}{\partial y}-\frac{1}{2}\frac{\partial Y_{yx}}{\partial x}+\frac{1}{2}\frac{\partial\left(Y_{zz}-Y_{yy}\right)}{\partial y}-\frac{1}{2}\frac{\partial^2 H_{zx}}{\partial x\partial y}-\frac{1}{2}\frac{\partial^2 H_{zy}}{\partial y^2} &= m_1\frac{\partial^2\phi_x}{\partial t^2}, \\ N_{yz}-\frac{\partial M_{xy}}{\partial x}-\frac{\partial M_{yy}}{\partial y}+\frac{1}{2}\frac{\partial\left(Y_{xx}-Y_{zz}\right)}{\partial x}+\frac{1}{2}\frac{\partial Y_{xy}}{\partial y}+\frac{1}{2}\frac{\partial^2 H_{xz}}{\partial x^2}+\frac{1}{2}\frac{\partial^2 H_{zy}}{\partial x\partial y} &= m_1\frac{\partial^2\phi_y}{\partial t^2}, \\ \frac{\partial \Xi_x}{\partial x}+\frac{\partial \Xi_y}{\partial y}+\Psi_z &= 0, \end{aligned} \tag{D.1}$$

where $\left(N_{ij},M_{ij}\right)=\int_{-h/2}^{h/2}\sigma_{ij}\left(1,z\right)dz$ are different integrals of Cauchy stress along the thickness direction of plate, $\left(Y_{ij},H_{ij}\right)=\int_{-h/2}^{h/2}m_{ij}\left(1,z\right)dz$ are different integrals of couple stress along the thickness direction of plate, $(\Psi_i,\Xi_i)=\int_{-h/2}^{h/2}D_i(1,z)dz$ are different integrals of electric displacement along the thickness direction of plate, and $(m_0,m_1)=(\rho h,\frac{\rho h^3}{12})$.